The global energy balance of the ASDEX Upgrade tokamak determined with the revised cooling water calorimetry

A. Redl,[1] T. Hohmann,[2] T. Eich,[2] N. Vianello,[3, 4] M. Bernert,[2] P. David,[2] N. den Harder,[2] A. Herrmann,[2] V. Rohde,[2] M. Weiland,[2] the ASDEX Upgrade Team,[a] and the EUROfusion MST1 Team[b]

[1)]*Universitá degli Studi della Tuscia, DEIM Department, Campus Riello, Blocco F, 01100 Viterbo, Italy*

[2)]*Max Planck Institute for Plasma Physics, Boltzmannstr. 2, 85748 Garching, Germany*

[3)]*Consorzio RFX (CNR, ENEA, INFN, Universitá di Padova, Acciaierie Venete SpA), Corso Stati Uniti 4, 35127 Padova, Italy*

[4)]*Istituto per la Scienza e la Tecnologia dei Plasmi, CNR, Padova, Italy*

(*Electronic mail: Andreas.Redl@unitus.it)

(Dated: 8 May 2023)

An extensive analysis of the global energy balance on the ASDEX Upgrade (AUG) tokamak has been performed. For such a purpose a complete revamping of the AUG cooling water calorimetry originally described in [T. Richter and H. Vernickel, Review of Scientific Instruments **65**, 5 (1994)] has been done. The system, which has been largerly improved, consists of 88 cooling units, which provides an almost perfect toroidal and poloidal coverage of the in-vessel components of the AUG tokamak. The analysis of the global energy balance based on almost 600 discharges reveal the remarkable capability to account more than 95 % of the total injected energy on average.

I. INTRODUCTION

The proper extrapolation of the energy loads on the different plasma facing components (PFCs) is of paramount importance for proper designs of future fusion power plants. Heat loads on PFCs can be caused by different mechanisms (plasma radiation, convective transport of charged or neutral particles) and different scenarios may exhibit different characteristics heat loads. Scaled up to next generation experiments [1, 2, 3, 4, 5, 6] such heat loads may become critical and may cause erosion or even permanent damage to the PFCs. Therefore, a reliable measurement of the energy distribution that covers completely the in-vessel components is needed to verify engineering assumptions.

With the construction of the AUG tokamak in the early 1990s, a unique calorimetry, dubbed Cooling Water Calorimetry (KWK) [7], encompassing the entire vessel was installed allowing to measure all 16 segments of the vacuum vessel separately. The cooling water calorimetry utilizes the relative rise in the inlet and outlet cooling water of the extensive cooling system to determine the heat loads in 88 different cooling units. However, this 1st generation setup suffered of several drawbacks including limited data acqisition time, high energy consumption and maintanance effort [8], and has therefore being abandoned in 2006. Over the last years, the signal acquisition has been entirely revamped while keeping the rest of the setup and evaluation method almost identical. This modernization allows to increase the performance of the system now able to resolve the temperature with an uncertainty of $\pm$ 0.03 K and a time resolution of 1 s. Given these peculiarities, the KWK will be used to infer the heat load on the different poloidal and toroidal sector of the AUG tokamak, aiming to

reproduce a proper energy balance on AUG. It is worth mentioning that the same exercise whenever tried on different devices [3, 9, 10, 11] so far, proved to be particularly difficult. The results presented hereafter will provide new insights into this interesting topic supporting the prediction of energy redistribution on PFCs of future devices.

The paper is structured as followed: in the section II A, the experimental setup of the calorimetry available at AUG is presented in detail. In section II B the underlying theoretical basis of the calorimetric evaluation for the energy deposited in each cooling unit is presented exploiting the modernized data acquitision [8] of the cooling water temperature profiles. The energy distribution of three different discharges obtained with the cooling water calorimery are shown and discussed in section II C. In section III, the first global energy balance of the AUG tokamak realized by means of the revised cooling water calorimetry is shown. Section IV summarizes the work and provides an outlook.

II. THE COOLING WATER CALORIMETRY AT AUG

A. The extensive cooling water system of the AUG tokamak

An extensive cooling water system covering the AUG tokamak has been installed at the time of its construction to ensure the proper cooling of all the components, both in-vessel as well of the supporting structures. Each of the 16 toroidal segments constituting the vessel shares a cooling circuit with an adjacent segment to cool the in-vessel components. In this system specific in-vessel components are cumulated to a cooling unit. Fig. 1 (top) gives an overview of the relevant cooling units, whereas Fig. 1 (bottom) provides a toroidal overview of the AUG tokamak indicating all three auxiliary heating devices operating at AUG. As indicated in Fig. 1 (bottom), the AUG Neutral Beam Injection (NBI) heating system has two NBI boxes with a total number of 8 sources. Fig. 1 (top)
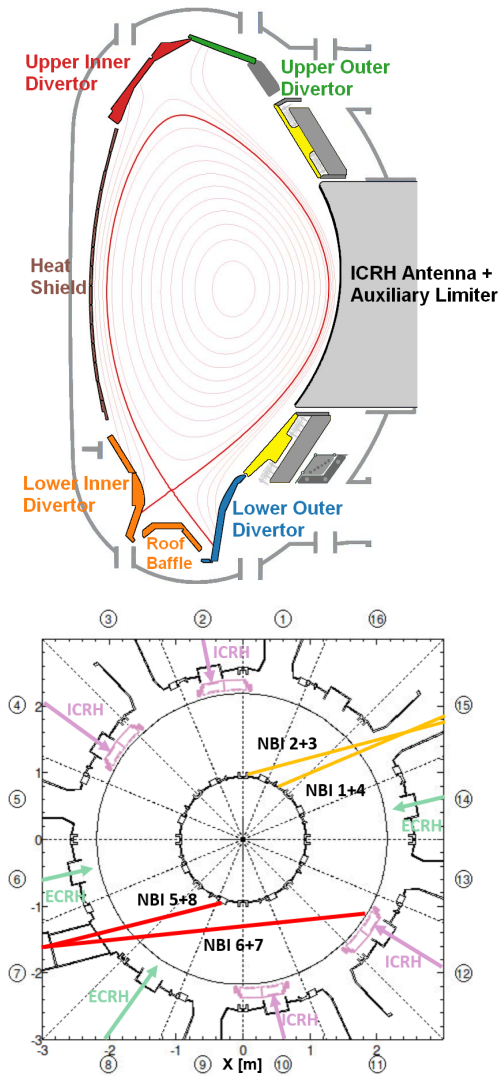
FIG. 1. Top: Poloidal cross section of AUG showing all installed cooling units. The cooling units highlighted by colored areas are installed in all 16 segments. It must be mentioned that the roof baffle is aligned to the cooling unit 'Lower Inner Divertor'. The cooling units labelled in black are installed in specific segments: the auxiliary limiters are installed in segment 6, 8, 14 and 16. The ICRH antennas are installed in segment 2, 4, 10 and 12. The tiles covering the PSL are highlighted in yellow. Bottom: Toroidal cross section of AUG indicating the position of the auxiliary heating devices NBI, Electron Cyclotron Resonance Heating (ECRH) and ICRH. The position of the ICRH antennas are added. The auxiliary limiters, installed on both side of each NBI box, are not indicated.

provides an overview of the installed cooling units denoted with colored areas which are encompassing these areas completely in toroidal direction. Each segment is equipped with five cooling units covering respectively the upper (inner/outer) divertor, the lower (inner/outer) divertor and the heat shield resulting in a total of 80 cooling units. It must be mentioned that the roof baffle is aligned to the cooling unit 'Lower Inner Divertor' due to changes in the divertor geometry since the 1st

generation setup. The cooling units indicated in black in Fig. 1 (top) are installed in specific segments. All PFCs of each Ion Cyclotron Resonance Heating (ICRH) antenna are connected to the cooling system, cumulated to one cooling unit and resolved individually. The ICRH antennas are installed in segment 2, 4, 10 and 12 and define the main limiter of the tokamak. The auxiliary limiters are installed in segment 6, 8, 14 and 16. One auxiliary limiter is installed at each side of the NBI duct and represents one cooling unit. Each auxiliary limiter is located radially slightly behind the main limiter in order to reduce heat loads on diagnostics. Totally, 88 cooling units are available, which cover almost entirely the vessel in poloidal and toroidal direction. Additionally, the tiles covering the passive stabilization loop (PSL, for more details to that in-vessel component we refer to Ref. [12]) are highlighted in yellow. Due to technical constraints, this part of the in-vessel components cannot be used for calorimetric studies.

Each segment has its own branch of the cooling circuit which supplies the colored cooling units in Fig. 1 and the cooling units of the auxiliary limiter in the respective segments. The inlet cooling tube is divided among the individual cooling units of the segment (see Fig. 2) and merged after leaving the tokamak vessel. Thermometers are installed in both,
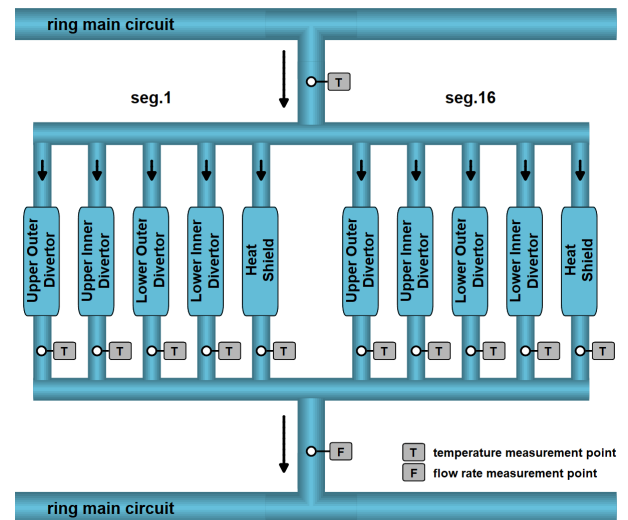

FIG. 2. Simplified illustration of the cooling circuit of two segments (here segment 1 and 16). From the ring main circuit, the inlet cooling water temperature is measured before the cooling water is distributed to the individual cooling units of each segment. After leaving the vessel, the temperature of the outlet cooling water of the respective cooling units is measured. After merging the individual cooling tubes, the flow rate of the segment is measured.

the inlet cooling tube (before branching) and outlet cooling tubes of the cooling units (after leaving the vessel). These thermometers are installed as close as possible to the experiment in order to minimize energy losses in the cooling water due to thermal transfer through the tubes to the environment (even though the tubes are thermally insulated outside the vessel). Platinum resistor thermometers PT-100 with a resolution of 0.03 K limited by the Simatic input card are used for measuring the cooling water temperature. The cooling units of the

ICRH antennas have their own cooling circuits in the respective segments. The setup is equipped with single flow rate meters and differential pressure transmitter in order to measure the flow rate of the outlet cooling water of each octant and the cooling circuits of the ICRH antenna. Recently, no further flow rate meters for single cooling units are installed. For any detailed description concerning the updated temperature measurements and data acquisition which is needed for the robust evaluation of the KWK, we refer to Ref. [8].

B. The underlying theory for the calorimetric evaluation of the cooling water system

To calculate the energy deposition per cooling unit Q, the formula as given in Ref. [7] has to be solved:

$$Q = m \int_{t_1}^{t_2} \Delta T c_p dt \tag{1}$$

For solving this integral several experimental inputs are needed:

- the heat capacity of the cooling water c_p, here 4184 $\frac{J}{kg \cdot K}$.

- the flow rate m for each cooling unit. At AUG, only for specific cooling circuits active flow rate measurements are available. Therefore, any flow rate has to be measured manually. For this purpose, a portable ultrasonic flowmeter, KATflow 200, is used. The used flow rates for all cooling units can be found in Ref. [13].

- the relative temperature ΔT, which is the difference of the inlet and outlet cooling water temperature.

- the time interval $[t_1, t_2]$, which has to cover the full excursion in the relative temperature profile ΔT.

As the discharge duration is short (max. 10 s), which is much smaller than the heat conduction time for the in-vessel components, no real-time data is available. Measuring the temperature signals during the cooling-down phase, allows only time-integrated results of the complete discharge.

For the proper determination of the relative temperature profile ΔT, the chosen time interval $[t_1, t_2]$ has to cover the full rise in the relative temperature ΔT in order to calculate correctly the energy deposition in each cooling unit. The temperature profiles may not cover the full cooling down phase. Fig. 3 shows an example of a not fully acquired decay profile. The red and green profiles represents the original ΔT-profile. The evaluation routine identifies the peak of the relative temperature profile ΔT and separate it into two profiles at a time point 75 s after the identified peak. The red profile in Fig. 3 represents the part of the profile until the separation and is simply numerically integrated. The green profile in Fig. 3 represents the profile after the separation and is used as fit reference for a double exponential fit defined as,

$$\Delta T(t) = T_0 \cdot \left(e^{-\kappa_{\text{cooling down, 1}} \cdot (t - t_{\text{sep}})} + e^{-\kappa_{\text{cooling down, 2}} \cdot (t - t_{\text{sep}})} \right), \tag{2}$$
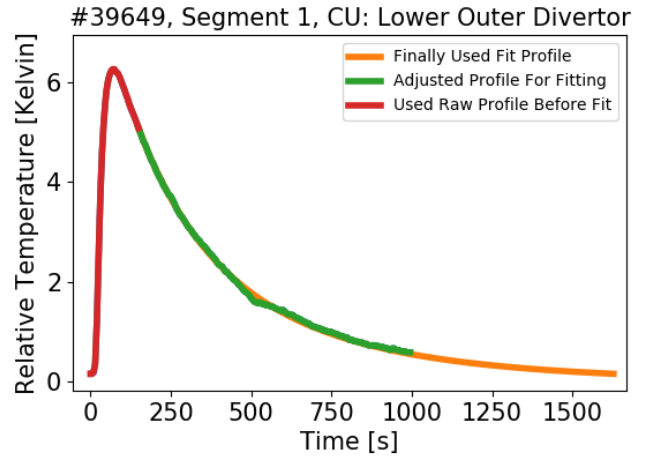

FIG. 3. Plot of the ΔT-profile for the cooling unit in the lower outer divertor in segment 1 for AUG discharge #39649. The green and red profile yield the original ΔT-profile. The orange curve represents the extrapolated fit function (according to Equ. (2)) providing the full decay profile required for the calculation of the deposited energy in this cooling unit.

where T_0, $\kappa_{\text{cooling down, 1}}$ and $\kappa_{\text{cooling down, 2}}$ have to be fitted. In case of the heat shield, a simpler fit function with just one exponential decay function is used. The parameter t_{sep} represents the time at the separation, T_0 the initial relative cooling water temperature at time t_{sep} and $\kappa_{\text{cooling down, 1/2}}$ cooling down coefficients. The limit of Equ. (2) is set to 0. The fit representing the decay profile is extrapolated until it reaches the initial temperature before the temperature rise. The orange profile in Fig. 3 represents such an extrapolated fit profile. This obtained profile is used for numerical integration in any cases. The sum of the integrated red profile and the orange profile yields the full energy deposited in a cooling unit.

An overall error of the evaluation can be estimated and is based on two uncertainties:

- the uncertainty in the measured flow rate, according to the manual ± 3 %

- the uncertainty in the acquired cooling water temperature profiles, here ± 0.03 K

The uncertainty of the flow rate meter is multiplied by 2 (meaning ± 6 %) in order to take into account that the required setup of the portable ultrasonic flow rate meter to measure the flow rate cannot be realized properly at all cooling tubes close to the AUG vessel due to the pipeline routing, leading to a larger uncertainty than provided by the manufacturer. As several mathematical operations are required to obtain the required ΔT-profile for Equ. (1), the overall uncertainty from this source is ± 0.12 K (for each mathematical operation we add the resolution uncertainty of ± 0.03 K). Both uncertainties are used as additional fit parameters in the fit routine for Equ. (2). The upper/lower error for all cooling units is the sum of the respective upper/lower error of each cooling unit yielding an estimated overall error of ± 6 %.
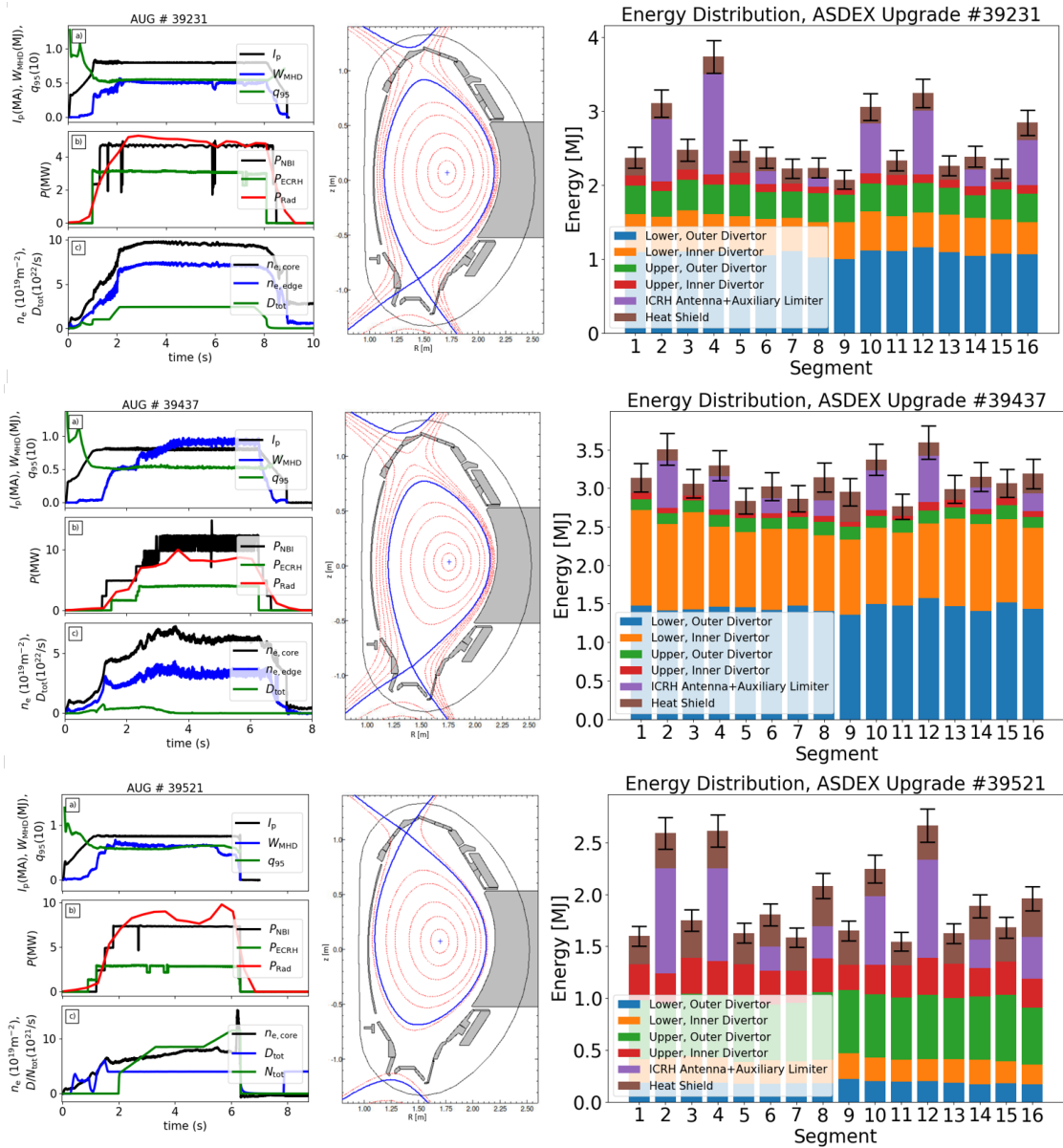
FIG. 4. Overview of time traces of main plasma parameter, equilibrium at t = 4.0 s and the energy distribution calculated with the cooling water calorimetry for three different scenarios: top row represents the quantities of a QCE discharge (for more information concerning this discharge, we refer to Ref. [14], the middle one of an AT discharge [15] and the bottom one of an USN discharge in CRD configuration (for more information concerning this scenario, we refer to Ref. [16]). For this discharge, the edge density $n_{e,edge}$ measured with the interferometer is not available. Instead, the nitrogen seeding rate N_{tot} is plotted. We want to emphasize that the scaling of the y-axis for each energy distribution is different.

C. First results of the energy distribution in ASDEX Upgrade

The AUG campaigns 2020/2021 and 2021/2022 are the first campaigns, in which measurements of the revised cooling water calorimetry have been acquired and evaluated. To illustrate the capabilities of the new calorimetric diagnostic, the time traces of main plasma parameters, the equilibrium and the energy distributions of three different discharge scenarios are discussed (overview given in Fig. 4). The plots of the first column show the time traces of specific plasma parameters, the middle column the equilibrium at time = 4.0 s and the third column the energy distribution obtained with the revised calorimetry. The first row illustrates the properties and results of a typical *Quasi-Continuous-Exhaust* (QCE) [17] discharge. The key properties of such a scenario are: operation with a high upper triangularity δ_{upper} leading to a equilibrium close-to-double-null (CDN) (we refer to the middle plot visualizing the equilibrium), high core and separatrix density $n_{e,core/sep}$ (see plot c) of first plot) and the absence of Type-I ELMs [18] associated to an enhanced filamentary transport in the far-SOL which dominates the radial transport at the midplane [17, 19].

These properties are consistent with the observations made with the cooling water calorimetry. The energy found on the lower inner divertor (orange bars) is lower compared to the one found on the lower outer divertor (blue bars). These conditions are compatible with a (partially) detachment of the inner divertor. We want to emphasize here that the cooling unit 'Lower Inner Divertor' consists of the PFCs of the lower inner divertor and roof baffle. The energy found on the lower inner divertor is expected to be significantly lower than given by the calorimetric value. At the same time, high heat load depositions can be found at the first wall (ICRH antennas and auxiliary limiters, purple bars) and the upper outer divertor (green bars) which confirms the presence of a significant radial heat transport likely caused by enhanced filamentary transport. These observations confirms previous studies in L- and H-modes [20, 21, 17, 19].

The middle row represents the properties and energy distribution of an *Advanced Tokamak* (AT) discharge [15]. Such scenarios require typically a low separatrix density $n_{e,sep}$ to maximize the current drive efficiency of ECRH and NBI and minimize the dependence on the toroidal plasma current I_p, combined with a high fraction of bootstrap current j_{BS} for non-inductively driven H-modes [15]. Due to the lower $n_{e,sep}$ and the presence of large Type-I ELMs, the lower inner divertor is attached. A significant fraction of heat loads can be measured by the calorimetry at the inner lower divertor confirming this property. The calorimetric measurements confirm that the heat loads on the first wall is even in the presence of Type-I ELMs quite low (compared to the totally calorimetric acquired heat loads). This observation indicates that the ratio between parallel and radial transport is different with respect to the previous scenario with more energy deposited into the inner and outer divertor.

The bottom row shows the properties and energy distribution of a *Compact Radiative Divertor* scenario [16] in upper single null (USN) configuration. This scenario is an alternative power exhaust solution for ITER and DEMO with shallow field line incidence angles at reasonable high power and promising confinement [16]. The key channel of power losses in such scenarios is radiation (radiative losses above 90 % can be achieved by developing a X-point-radiator [22]). Even for such a dedicated discharge with dominating radiative fraction, the calorimetry can resolve a reasonable distribution. A significant fraction of the injected energy goes on the upper divertor consistent with the fact that the configuration is in USN. The energy deposition in the upper divertor is concentrated on the upper outer divertor consistent with the strikeline and X-point configuration (we refer to the middle plot visualizing the corresponding equilibrium) in this dedicated scenario. We want to clarify here that the calorimetry cannot discriminate between particle and radiation caused heat loads. Strong radiative losses can cause significant heat loads on any PFCs which is properly acquired by the revamped calorimetry.

III. ENERGY BALANCE IN ASDEX UPGRADE

A proper energy balance requires the determination of all possible energy sources and losses according to the following:

$$E_{OH} + E_{NBI} + E_{ECRH} + E_{ICRH} =$$
$$E_{Calorimetry} + E_{Rad, Limiter+PSL} + E_{NBI\text{-}losses}, \qquad (3)$$

where the terms on the left-hand side denotes the energy input accounting all possible heating possibilities available on AUG. Since the ohmic heating power is measured from the plasma itself, no heating efficiency has to be supposed. For the NBI contribution, the totally injected energy is used. In case of the ECRH and ICRH contribution, a 100 % coupling-efficiency is supposed. The first contribution on the right-hand side of Equ. (3) represents the sum of the energy loads of all in-vessel components obtained with the revised cooling water calorimetry. $E_{Rad, Limiter+PSL}$ denotes the part of radiation energy which cannot be acquired by the cooling water calorimetry and has to be simulated. At AUG, the cooling water calorimetry is neither able to acquire the energy deposited in the limiter shadow (the area between the four ICRH antennas and the auxiliary limiters) nor the energy deposited at the PSL. We assume that both areas are mainly heated up by radiation. The final contribution $E_{NBI\text{-}losses}$ summarizes the contributions of the NBI shine-through, NBI orbit and NBI charge-exchange (CX) losses, which individually may be small but in sum may have an impact on the global energy balance. The most of the NBI shine through is properly counted by the revised calorimetry, except of the NBI beams 6 and 7, which are tangentially oriented (for illustration we refer to Fig. 1). Any shine through will partially reach the PSL, an area which cannot be used for calorimetric studies. We assume that most of the latter two losses are deposited on the low-field side, where the revised calorimetry has the poorest coverage, resulting in low acquisition of these losses. The NBI-losses are calculated with the code RABBIT [23] and the fraction of the shine through reaching the PSL is estimated with the code ABC3D [24].

In order to estimate the radiative heat loads for both areas (limiter shadow and PSL), the simulation code CHERAB [25] is used. CHERAB is mainly used for spectroscopic plasma emission simulations, but is also able to simulate, given a prescribed radiative source, the radiative heat loads on any PFCs. Fig. 5 shows the setup realized for the AUG tokamak in CHERAB for an experimental 2D emissivity profile determined from the AUG bolometry (Fig. 5 (left column, top)) and the poloidal radiative heat load distribution of the AUG PFCs (Fig. 5 (left column, bottom)) obtained with that profile. The starting point and direction of the evaluation scheme for the poloidal distribution of the radiative heat loads is indicated in the top plots. In the upper plots, the black line represents the 2D-poloidal contour of the AUG vessel and in-vessel components. The blue line denotes the so-called 'synthetic wall detectors'. These detectors are implemented for the determination of the radiative power reaching the respective area. For counting the fraction of radiative power reaching each synthetic wall detector the code CHERAB exploits the Python package raysect using the ray-tracing approach [26]. These
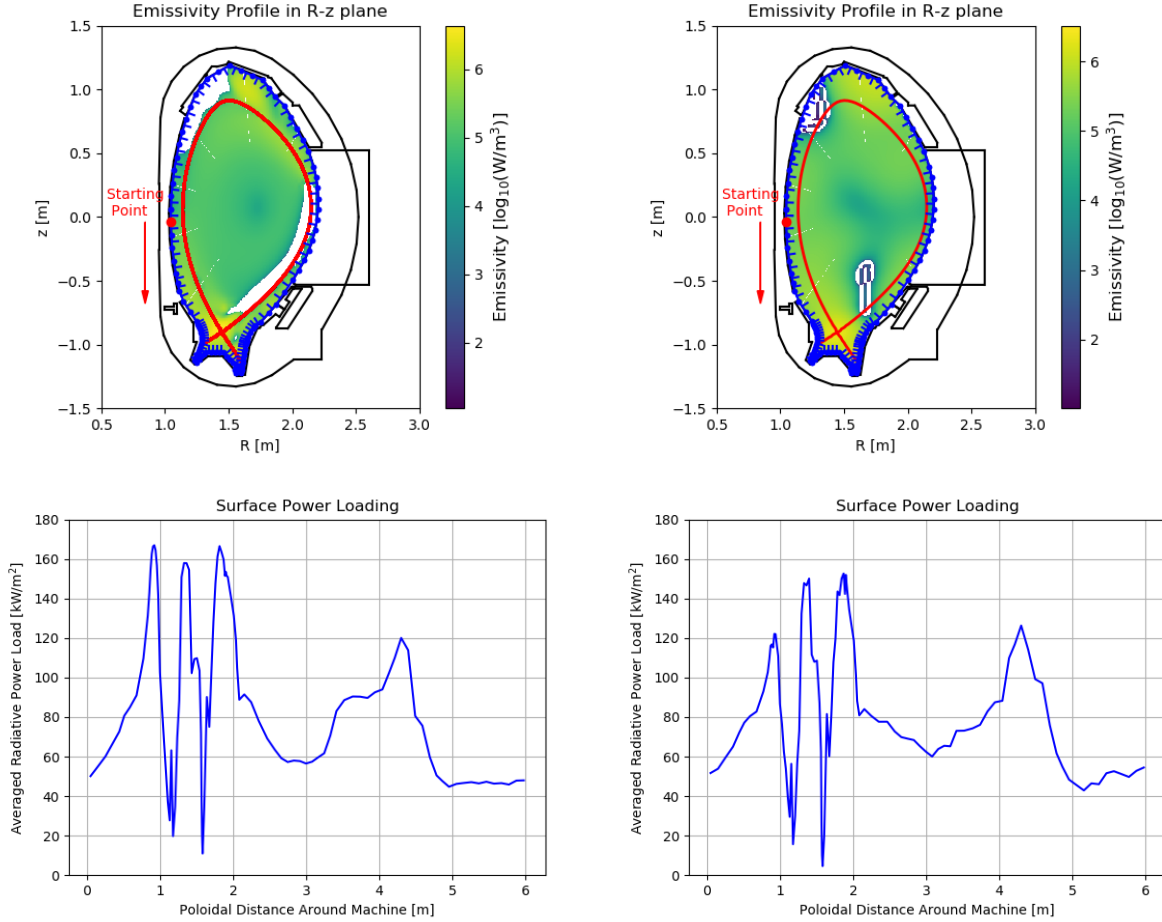
FIG. 5. Overview of the setup used in CHERAB in order to assess the poloidal distribution of radiative heat loads for discharge #39231: left column with experimental 2D emissivity profile and obtained poloidal radiative heat load distribution, right column with simplified synthetic 2D emissivity profile and obtained poloidal radiative heat load distribution. The starting point and direction of the evaluation scheme is indicated in each top plot.

wall detectors follow the entire contour of the AUG in-vessel components with a small offset (magnitude 1mm) to ensure numerical stability.

To obtain the amount of radiative energy at any PFCs for a large database, a systemic approach has to be used. The standard tomography method (example is shown in Fig. 5 (left column)) used at AUG requires manual optimization of parameters for each reconstruction and is therefore not suited for automatic computation over large sample of data [27]. Instead, a recently developed Gaussian process tomography (GPT) was used [28]. This model uses a set of hyperparameters which is trained with Gaussian process tomography (GPT) on a database of 75 experimental emission distributions considering different AUG scenarios. For this study, the hyperparameters for the Cartesian kernel funtion were used. The bolometric input values are median averaged with a temporal resolution of 1 ms. The radiative contribution is integrated in time with a time resolution of 2 ms.

The newly obtained emissvity profile and the poloidal distribution of the radiative heat loads can be found in Fig. 5 (right column). One can clearly see that the distribution based on the GPT model is close, but not equal to the experimental one. The largest discrepancy is identified at the lower inner divertor, where $\sim$ 75 % of the experimentally expected radiative power can be found. To obtain the incident radiative energy at the PSL for the entire tokamak vessel surface, the values determined for the respective wall detector covering the PSL are extended to the full toroidal circumference, integrated in time and summed up. In case of the limiter range, the same procedure is done but excluding the fraction of the limiter area which is covered by the four ICRH antennas.

With all these informations one can fill up the right-hand side of Equ. (3). Next to this, estimated errors of the input energy and of the calculated heat loads on the PFCs can be provided:

- NBI: $\pm$ 5 %

- ECRH: $\pm$ 5 %

- ICRH: $\pm$ 5 %

- Ohmic Heating: $\pm$ 5 %

- Calorimetry: $\pm\, 6\,\%$

- Radiation: $\pm\, 8.8\,\%$

Due to the complexity of the external heating methods, an exact determination of the uncertainties cannot be realized (with respect to this challenge, we refer to Ref. [3]). The uncertainty of the ohmic heating is based on the uncertainties of the measurement setup of the Rogowski coils and the toroidal conductor loop. In case of the KWK, the uncertainty was estimated in this manuscript. For the bolometric measurements, we refer for the uncertainty to Ref. [27]. Uncertainties of the experimental tomographic reconstructions used to train the GPT model and the uncertainties of the CHERAB computation cannot be properly quantified.

Fig. 6 (top) presents the global energy balance of AUG realized with a database of almost 600 discharges from the second half of the 2020/2021 campaign and the full 2021/2022 campaign. The x-axis of Fig. 6 (top) represents the sum of the left side of Equ. (3), whereas the y-axis represents the sum of the right side of Equ. (3). The dashed bold bisector represents the goal of 100 % detection. A colormap is added visualizing the simulated radiation energy normalised against the injected energy. This database covers a large range of different scenarios (different equilibrium configurations, different seeding gases (N, Ne, Ar, He), different heating schemes, different fuelling levels including pellet fuelling and different main gases (D, He)), which have been executed in the last two campaigns at AUG and a large range in injected energy, starting from ~ 5 MJ up to ~ 100 MJ. The thin dashed line represents the detection rate obtained from a linear regression between input energy and detected energy. According to the applied linear regression the presented setup is able to find 95 % of the input energy on average for various, strongly different discharge scenarios and fractions of simulated radiated energy. Additionally, the mean error based on the sum of the individual uncertainties of each contribution is determined for the entire database. The mean error reveal a low scatter in both directions (± 5.0 % in x-direction and ± 8.8 % in y-direction) supporting the reliability of the AUG global energy balance.

Fig. 6 (middle) and (bottom) visualize the individual contributions to the global energy balance according to Equ. (3), starting with the heating contributions (middle) of the left-hand side of Equ. (3). The bottom plot illustrates the three contributions (the energy measured with the calorimetry, the fraction of simulated radiative energy reaching the limiter shadow and the PSL and contributions related to NBI losses) which can be found on the right-hand side of Equ. (3). According to the plots, one can identify that the simulated radiative fraction for the right side of Equ. (3) is relevant due to its significance in the energy balance for any input energy (the entire radiation energy $E_{Rad,tot}$ is added in the bottom plot as comparison for the simulated contribution). The simulated radiative contribution is in the presented database in the magnitude of ECRH contributions.

The contribution $E_{NBI\text{-losses}}$ includes as introduced the contributions of the NBI shine through which reaches the PSL, the NBI orbit and the NBI CX losses. While The first contribution can accurately be determined with the aid of RABBIT
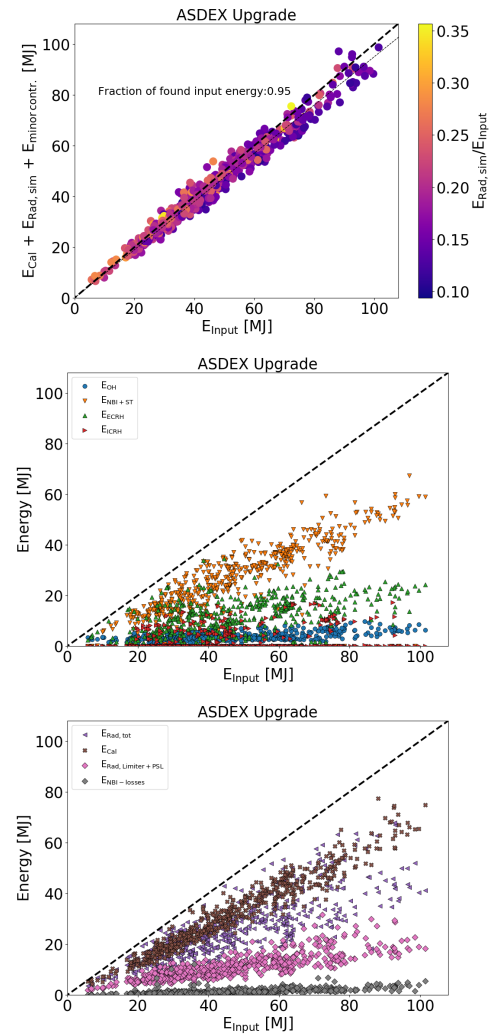

FIG. 6. Top: Visualization of the global energy balance obtained with the opimized cooling water calorimetry at the AUG tokamak. The x-axis represents the left-hand side of Equ. 3, whereas the the y-axis represents the right-hand side of that equation. A colormap is added representing the fraction of simulated radiative energy normalised against the injected energy for each discharge. Applying a linear regression on that database, one yields a detection rate of 95 % of the input energy. Middle: Visualization of each contributor to the global energy balance of the left-hand side of Equ. 3. The four contributions represent the injected energy of each heating system available at AUG. Bottom: Visualization of each contributor to the global energy balance of the right-hand side of Equ. 3. The three contributions represent the calorimetrically captured energy, the simulated radiative energy reaching the limiter shadow and the PSL and contributions related to NBI losses. Additionally, the total radiative energy taken from the foil bolometry [27] is added as comparison for the simulated contribution.

and ABC3D, this does not apply to the two latter contributions. Both input and calculations are subject to certain assumptions [23, 29, 30]. RABBIT only calculates first-orbit losses, the subsequent collision-induced orbit losses are not considered. Furthermore, robust CX loss calculations would require the proper determination of the neutral particle den-

sity, which is hard to obtain for a large database, because it is not directly measured. For this analysis, the same fit profile for the neutral particle density is used in all discharges. In this study, both contributions for the entire database contribute on average $\sim$ 3 % to the energy balance (see Fig. 6 (bottom)). However, studies on TCV [31] and more recently on JET [32] have shown that NBI losses can be significant and an adequate in-depth analysis of NBI losses to the energy balance may be beneficial.

A reasonable agreement between injected and detected energy with low scatter in x- and y-direction have been presented. The mean discrepancy between input and detected energy is according the applied linear regression $\sim$ 5 %. The large database reflects that the calorimetry can capture between 60 % and 85 % of the total injected energy for arbitrary plasma scenarios. The calorimetric diagnostic thus represents the main contributor for any plasma scenarios of the AUG tokamak for the right-hand side of Equ. (3). The great effort in improving the data resolution and maximizing the acquisition time [8] together with a reasonable extrapolation fit is the basis for robust values for arbitrary plasma scenarios. The lower limit of the energy captured by the KWK is given by CRD scenarios, which have a dominating radiative fraction (> 90 %) [33]. The high radiation fraction for such discharges is also reflected by high heat loads found with the limiter cooling units (purple bars) in Fig. 5 (third column, bottom plot). At the same time, the radiative component provided by means of CHERAB and a GPT-model acts as a key contributor, as its contribution can vary between 10 % and up to 35 % (corresponding to the values in Fig. 6 (top)), thus encompassing a significant range of the injected energy. This broad contribution to the energy balance strongly emphasizes the need for accurate and reliable calculations of radiative losses for the areas around the limiter and the PSL which the AUG calorimetry, despite its very good coverage, cannot capture.

With the establishment of the energy balance using the revised KWK, a novel approach based on the code CHERAB and a simple GPT model for bolometric reconstruction in order to accurately determine the radiative fraction has been introduced. The results derived with both codes coincide well with results based on bolometric reconstructions (see Fig. 5) and are suitable for a reasonable calculation of the key contribution for any plasma scenario. In previous studies at AUG [10, 9], JET [34] and EAST [35] facing the global energy balance challenge, an approbriate determination of radiative losses realised by means of bolometric measurements have not been realised. So far, simplifications, like constant correction factors, were applied on databases in order to take into account radiative losses. The AUG results of the CHERAB framework impressively show that the radiation losses can vary widely for a large database and radiative losses require a shot-by-shot assessment.

The capabilities of the revamped calorimetry are not limited to establishing the global energy balance in order to confirm engineering assumptions, but are also suitable for trustworthy heat load studies. Calorimetric measurements with such high spatial coverage can be useful as a supportive diagnostic for scenario development focused on power exhaust solutions and

contributes already in CRD-studies [16]. The properties and the energy distribution of such a scenario are shown in Fig. 4 (bottom row). With the help of dedicated plasma discharges in order to investigate the impact of filamentary energy transport the AUG calorimetry have provided the key observation to identify the parameter suitable to scale the first wall heat loads [14]. Such special discharges can also be studied to analyze the inner/outer asymmetry in the divertor (previous studies on this topic were performed at JET [36]), which are also useful as input for numerical simulations.

With its very good toroidal and poloidal coverage, the revised cooling water calorimetry allows promising analyses of possible toroidal asymmetries (not only the divertor region) on a segmental resolution (such studies have already been pointed out in Ref. [7] and recently in Ref. [37] giving new insights to the challenge of toroidal asymmetry) accepting certain limitations on the minimum spatial resolution. Diagnostics measuring the heat flux with higher spatial and temporal resolution, such as IR thermography, Langmuir probes and thermocouples usually have a limited toroidal coverage. The synergy between calorimetry and high temporal resolution diagnostics allow to cross check the results from heat load measurement against the energy input measured by the calorimetry.

The results obtained so far at AUG and possible applications underline the importance of coolant-based calorimetries also for future experiments (ITER and DEMO). As an additional application for long-run pulses, monitoring of heat fluxes at any PFCs can be added, an aspect with respect to the unsolved power exhaust challenge still has its importance. The operation of such calorimetries in long-run pulses, as foreseen in ITER or DEMO cannot be tested in AUG, but rather in devices like EAST [35], WEST [38] and soon in JT60-SA operating with superconducting coils. The monitoring of heat fluxes (the monitoring of α-heating cannot be properly tested in current devices) at any PFCs of a discharge is mandatory for the safe operation of the next generation tokamaks and have to be tested in the currently available tokamaks capabable to operate with long-run pulses. The WEST tokamak is already extensively equipped with dedicated ITER-like components with cooling tubes installed within tiles [38] and ideal to test the implementation of different techniques (minimum spatial resolution, coverage of in-vessel components, installation/location of measurement points, use of industrial components, realization of data acquisition/evaluation/interpretation, maintenance/repair effort) for the next generation devices.

IV. SUMMARY

A revamped calorimetric diagnostic is now routinely available at the AUG tokamak, comprising an experimental setup that almost completely covers the AUG vessel in poloidal and toroidal direction(section II A) consisting of 88 cooling units. Cooling units represent the smallest spatial resolution to resolve heat loads. The underlying evaluation methodology (Equ. (1)), based on the findings of the 1st generation setup and optimized for the new setup, has been presented in detail using an example temperature profile (II B). Due

to short pulse lengths, no real-time information can be provided, just time-integrated. Energy distributions of three different scenarios (Fig. 4), namely a *Quasi-continuous-exhaust*, an *Advanced Tokamak* and a *Compact radatiave divertor* scenario, have been extensivley discussed demonstrating the capabilities and importance of this diagnostic for any heat load studies. Based on these promising results, an attempt to establish the still challenging global energy balance has been made. The inputs on the left and right sides of Equ. (3) are determined properly. The contributors of the left-hand side of Equ.(3) corresponds to the injected energy provided by four different heating systems (OH, NBI, ECRH and ICRH). With focus on the right side of Equ. (3), two main contributors are identified: the energy acquired by the entire calorimetry (corresponding to the sum of 88 cooling untis) and a radiative contribution needed for the PSL and the limiter shadow both determined by a novel framework based on the code CHERAB and on a GPT-based bolometric reconstruction model. Applying a linear regression on the database of ~ 600 discharges (Fig. 6) using the values on the left and right sides of Equ. (3), a promising detection rate of 95 % on average has been obtained. The contributions of calorimetry vary between 60 % and 85 % of the injected energy, while the contribution of radiation can vary between 10 % and 35 %. Both, the revamped cooling water calorimetry and the simulated radiative fraction provide in sum, a satisfactory calculation of the global energy balance of the AUG tokamak. Further applications of this promising diagnostic setup for future studies have been discussed. Such a simple, but robust diagnostic is suitable for heat loads studies (likely power exhaust scenario development [33]), toroidal asymmetries [37] or even for quantification of transport phenomena [14]. The simple design combined with low maintenance due to standardized industrial components for data acquisition make this coolant-based calorimetry a promising and easy-to-use diagnostic that may also be of interest to monitore the energy distribution onto in-vessel components and to cross check high time resolution heat load measurements by comparing the time intergrated values with calorimetric data in ITER and DEMO.

REFERENCES

[1] T. Eich, A. Leonard, R. Pitts, W. Fundamenski, R. Goldston, T. Gray, A. Herrmann, A. Kirk, A. Kallenbach, O. Kardaun, A. Kukushkin, B. LaBombard, R. Maingi, M. Makowski, A. Scarabosio, B. Sieglin, J. Terry, A. Thornton, the ASDEX Upgrade Team, and the JET EFDA Contributors, Nuclear Fusion **53**, 0930310 (2013).

[2] T. Eich, B.Sieglin, A. Thornton, M. Faitsch, A. Kirk, A. Herrmann, W. Suttrop, the JET contributors, the MST contributors, the ASDEX Upgrade, and the MAST teams, Nuclear Materials and Energy **12**, 84–90 (2017).

[3] G. F. Matthews, P. Bunting, S. Devaux, P. Drewelow, C. Guillemaut, D. B. King, E. Lerche, S. Silburn, G. Szepesi, V. Riccardo, V. Thompson, and J. Contributors, Nuclear Materials and Energy **12**, 227–233 (2017).

[4] A. Loarte, G. Huijsmans, S. Futatani, L. Baylor, T. Evans, D. M. Orlov, O. Schmitz, M. Becoulet, P. Cahyna, Y. Gribov, A. Kavin, A. S. Naik, D. Campbell, T. Casper, E. Daly, H. Frerichs, A. Kischner, R. Laengner, S. Lisgo, R. Pitts, G. Saibene, and A. Wingen, Nuclear Fusion **54**, 033007 (2014).

[5] G. Federici, A. Loarte, and G. Strohmayer, Plasma Physics and Control. Fusion **45**, 1523 (2003).

[6] G. Federici, C. Bachmann, L. Barucca, C. Baylard, W. Biel, L. Boccaccini, C. Bustreo, S. Ciattaglia, F. Cismondi, V. Corato, C. Day, E. Diegele, T. Franke, E. Gaio, C. Gliss, T. Haertl, A. Ibarra, J. Holden, G. Keech, R. Kembleton, A. Loving, F. Maviglia, J. Morris, B. Meszaros, I. Moscato, G. Pintsuk, M. Siccinio, N. Taylor, M. Tran, C. Vorpahl, H. Walden, and J. You, Nuclear Fusion Fusion **59**, 066013 (2019).

[7] T. Richter and H. Vernickel, Review of Scientific Instruments **65**, 1613 (1994).

[8] T. Hohmann, A. Redl, V. Rohde, G. Schall, M. Schandrul, and the ASDEX Upgrade Team, Fusion Engineering and Design **187**, 113365 (2023).

[9] A. Herrmann, T. Eich, V. Rohde, C. J. Fuchs, J. Neuhauser, and the ASDEX Upgrade Team, Plasma Physics and Controlled Fusion **46**, 971 (2004).

[10] J. C. Fuchs, T. Eich, A. Herrmann, K. Mast, and the ASDEX Upgrade Team, Journal of Nuclear Materials **337–339**, 756–760 (2005).

[11] M. Bernert, T. Eich, A. Kallenbach, D. Carralero, A. Huber, P. T. Lang, S. Potzel, F. Reimold, J. Schweinzer, E. Viezzer, H. Zohm, and the ASDEX Upgrade Team, Plasma Physics and Controlled Fusion **57**, 014038 (2015).

[12] C. Vorpahl, W. Suttrop, M. Ebner, B. Streibl, H. Zohm, and the ASDEX Upgrade Team, Fusion Engineering and Design **88**, 537–540 (2013).

[13] A. Redl, T. Hohmann, T. Eich, N. Vianello, M. Bernert, P. David, N. den Harder, A. Herrmann, V. Rohde, M. Weiland, the ASDEX Upgrade Team, and the EUROfusion MST1 Team, "The global energy balance of the asdex upgrade tokamak determined with the revised cooling water calorimetry," Zenodo **https://doi.org/10.5281/zenodo.6368069** (2022).

[14] A. Redl, T. Eich, N. Vianello, P. David, the ASDEX Upgrade Team, and the EUROfusion MST1 Team, Nuclear Materials and Energy **34**, 101319 (2023).

[15] A. Bock, E. Fable, R. Fischer, M. Reich, D. Rittich, J. Stober, M. Bernert, A. Burckhart, H. Doerk, M. Dunne, B. Geiger, L. Giannone, V. Igochine, A. Kappatou, R. McDermott, A. Mlynek, T. Odstrčil, G. Tardini, H. Zohm, and the ASDEX Upgrade Team, Nuclear Fusion **57**, 126041 (2017).

[16] T. Lunt, M. Bernert, D. Brida, P. David, M. Faitsch, O. Pan, A. Redl, D. Stieglitz, U. Stroth, and the ASDEX Upgrade Team, submitted to Physical Review Letters (2023).

[17] M. Faitsch, T. Eich, G. F. Harrer, E. Wolfrum, D. Brida, P. David, M. Griener, U. Stroth, the ASDEX Upgrade Team, and the Eurofusion MST1 Team, Nuclear Materials and Energy **26**, 100890 (2021).

[18] F. Wagner, G. Fussmann, T. Grave, M. Keilhacker, M. Kornherr, K. Lackner, K. McCormick, E. Müller, A. Stäbler, G. Becker, K. Bernhardi, U. Ditte, A. Eberhagen, O. Gehre, J. Gernhardt, G. Gierke, E. Glock,

O. Gruber, G. Haas, M. Hesse, G. Janeschitz, F. Karger, S. Kissel, O. Klüber, G. Lisitano, H. Mayer, D. Meisel, V. Mertens, H. Murmann, W. Poschenrieder, H. Rapp, H. Röhr, F. Ryter, F. Schneider, G. Siller, P. Smeulders, F. Söldner, E. Speth, K.-H. Steuer, Z. Szymanski, and O. Vollmer, Physical Review Letters **53**, 1453 (1984).

[19] N. Vianello, D. Carralero, C. Tsui, V. N. M. Agostini, I. Cziegler, B. Labit, C. Theiler, E. Wolfrum, D. Aguiam, S. Allan, M. Bernert, J. Boedo, S. Costea, H. D. Oliveira, O. Fevrier, J. Galdon-Quiroga, G. Grenfell, A. Hakola, C. Ionita, H. Isliker, A. Karpushov, J. Kovacic, B. Lipschultz, R. Maurizio, K. McClements, F. Militello, A. Nielsen, J. Olsen, J. Rasmussen, T. Ravensbergen, H. Reimerdes, B. Schneider, R. Schrittwieser, E. Seliunin, M. Spolaore, K. Verhaegh, J. Vicente, N. Walkden, W. Zhang, the ASDEX Upgrade Team, the TCV Team, and the EUROfusion MST1 Team, Nuclear Fusion **60**, 016001 (2020).

[20] D. Carralero, S. Artene, M. Bernert, G. Birkenmeier, M. Faitsch, P. Manz, P. de Marne, U. Stroth, M. Wischmeier, E. Wolfrum, the ASDEX Upgrade Team, and the EURO-fusion MST1 Team, Nuclear Fusion **58**, 096015 (2018).

[21] G. Birkenmeier, P. Manz, D. Carralero, F. Laggner, G. Fuchert, K. Krieger, H. Maier, F. Reimold, K. Schmid, R. Dux, T. Pütterich, M. Willensdorfer, E. Wolfrum, and the ASDEX Upgrade Team, Nuclear Fusion **55**, 033018 (2015).

[22] M. Bernert, F. Janky, B. Sieglin, A. Kallenbach, B. Lipschultz, F. Reimold, M. Wischmeier, M. Cavedon, P. David, M. Dunne, M. Griener, O. Kudlacek, R. McDermott, W. Treutterer, D. Brida, O. Fevrier, S. Henderson, M. Komm, the EUROfusion MST1 team, and the ASDEX Upgrade Team, Nuclear Fusion **61**, 024001 (2021).

[23] M. Weiland, R. Bilato, R. Dux, B. Geiger, A. Lebschy, F. Felici, R. Fischer, D. Rittich, M. van Zeeland, the ASDEX Upgrade Team, and the Eurofusion MST1 Team, Nuclear Fusion **58**, 082032 (2018).

[24] N. den Harder, D. Rittich, G. Orozco, and C. Hopf, Plasma Physics and Controlled Fusion **62**, 025023 (2020).

[25] C. Giroud, A. Meakins, M. Carr, A. Baciero, and C. Bertrand, "Cherab spectroscopy modelling framework (version v0.1.0)," Zenodo **http://doi.org/10.5281/zenodo.1206142** (2018).

[26] M. Carr, A. Meakins, M. Bernert, P. David, C. Giroud, J. Harrison, S. Henderson, B. Lipschultz, F. Reimold, the EUROfusion MST1 Team, and the ASDEX Upgrade Team, Review of Scientific Instruments **89**, 083506

(2018).

[27] P. David, M. Bernert, T. Pütterich, C. Fuchs, S. Glöggler, T. Eich, and the ASDEX Upgrade Team, Nuclear Fusion **61**, 066025 (2021).

[28] K. Moser, A. Bock, P. David, M. Bernert, R. Fischer, and A. U. Team, Fusion Science and Technology **78**, 607–616 (2022).

[29] K. Bogar, B. Geiger, P. Schneider, A. J. van Vuuren, O. Grover, the ASDEX Upgrade Team, and the EUROfusion MST1 Team, Nuclear Fusion **61**, 036001 (2021).

[30] M. Weiland, R. Bilato, B. Sieglin, F. Felici, L. Giannone, O. Kudlacek, M. Rampp, M. Scheffer, W. Treutterer, and T. Zehetbauer, Nuclear Fusion **accepted** (2023).

[31] B. Geiger, A. Karpushov, B. Duval, C. Marini, O. Sauter, Y. Andrebe, D. Testa, M. Marascheck, M. Salewski, P. Schneider, the TCV Team, and the EUROfusion MST1 Team, Plasma Physics and Controlled Fusion **59**, 115002 (2017).

[32] D. B. King, R. Sharma, C. Challis, A. Bleasdale, E. Delabie, D. Douai, D. Keeling, E. Lerche, M. Lennholm, J. Mailloux, G. Matthews, M. Nicassio, Z. Stancar, T.Wilson, and J. contributors, submitted to Nuclear Fusion Special Issue (2023).

[33] T. Lunt, H. Frerich, D. Brida, D. Carralero, M. Cavedon, A. Drenik, M. Faitsch, Y. Feng, M. Griener, A. Herrmann, B. Kurzan, O. Pan, U. Plank, D. Silvagni, M. Willensdorfer, M. Wischmeier, E. Wolfrum, and the ASDEX Upgrade Team, Plasma Physics and Controlled Fusion **62** (2020).

[34] G. F. Matthews, S. K. Erents, W. Fundamenski, C. Ingesson, R. Monk, and V. Riccardo, Journal of Nuclear Materials **290-293**, 668–672 (2001).

[35] Q. Zhuang, T. Ming, Y. Yu, Y. Liu, L. Yang, F. Long, Q. Shi, B. Li, S. Liu, H. Liu, G. Li, and X. Gao, Physica Scripta **97**, 095602 (2022).

[36] T. Eich, P. Andrew, A. Herrmann, W. Fundamenski, A. Loarte, R. A. Pitts, and the JET-EFDA contributors, Plasma Physics and Controlled Fusion **49**, 573–604 (2007).

[37] V. Rohde, M. Balden, K. Hunger, R. Neu, I. Zammuto, A. Herrmann, K. Hegele, and the ASDEX Upgrade Team, Nuclear Materials and Energy **34**, 101329 (2022).

[38] J. Gaspar, Y. Corre, N. Fedorczak, J. Gunn, C. Bourdelle, S. Brezinsek, J. Bucalossi, N. Chanet, R. Dejarnac, M. Firdaouss, J.-L. Gardarein, G. Laffont, T. Loarer, C. Pocheau, E. Tsitrone, and the WEST Team, Nuclear Fusion **61**, 096027 (2021).